Characterizing the Swimming Properties of Artificial Bacterial Flagella

Li Zhang,*,† Jake J. Abbott,†,‡ Lixin Dong,†,§ Kathrin E. Peyer,†
Bradley E. Kratochvil,† Haixin Zhang,† Christos Bergeles,†
and Bradley J. Nelson*,†

Institute of Robotics and Intelligent Systems, ETH Zurich, CH-8092 Zurich, Switzerland, Department of Mechanical Engineering, University of Utah, Salt Lake City, Utah 84112, and Department of Electrical and Computer Engineering, Michigan State University, East Lansing, Michigan 48824

ABSTRACT

Artificial bacterial flagella (ABFs) consist of helical tails resembling natural flagella fabricated by the self-scrolling of helical nanobelts and soft-magnetic heads composed of Cr/Ni/Au stacked thin films. ABFs are controlled wirelessly using a low-strength rotating magnetic field. Self-propelled devices such as these are of interest for in vitro and in vivo biomedical applications. Swimming tests of ABFs show a linear relationship between the frequency of the applied field and the translational velocity when the frequency is lower than the step-out frequency of the ABF. Moreover, the influences of head size on swimming velocity and the lateral drift of an ABF near a solid boundary are investigated. An experimental method to estimate the propulsion matrix of a helical swimmer under a light microscope is developed. Finally, swarm-like behavior of multiple ABFs controlled as a single entity is demonstrated.

It is well known that a variety of micro-organisms swim in liquid using flagella. Flagellar mechanisms are particularly well suited to a low-Reynolds-number regime because of their ability to generate nonreciprocating motion.[1] Eukaryotic flagella are active organelles that deform to create paddling motions such as traveling waves.[2] Previous work experimentally demonstrated that this kind of motion can be approximated by a microscopic artificial swimmer consisting of a chain of DNA-bound magnetic beads connected to a red blood cell.[3] In contrast, bacterial (prokaryotic) flagella work differently by using a molecular motor to turn the base of a flagellum or bundle of flagella that form a helical structure.[4] Inspired by the natural design of bacterial flagella, we previously reported artificial bacterial flagella (ABFs) that have comparable geometries and dimensions to their organic counterparts and can swim in a controllable fashion in three-dimensions (3D) using weak applied magnetic fields.[5] ABFs represent the first demonstration of artificial swimmers that use helical nanobelt propulsion. They provide a 6-degree of freedom (6-DOF) micro- and nanomanipulation tool for manipulating cellular or subcellular objects, for sensing and transmitting inter- or intracellular information, and for targeted drug delivery. However, the relationship between

velocity, angular speed, and the frequency of the applied field remains unclear. Moreover, the influence of the head size of the ABF on the swimming velocity must be investigated in order to optimize swimming performance. In this report, these swimming properties are characterized quantitatively by experiments and analyzed by a simplified mathematical model based on a spherical head and a helical wire. In addition, the propulsion matrix[1,6,7] of ABFs is explored, by which the magnetic torque, the swimming velocity, and the maximum propulsion efficiency can be estimated from a given frequency of the rotating magnetic field. Self-propelled devices such as these are of interest in fundamental research and for biomedical applications.[5,8−12] Magnetic approaches have the advantage that they do not require high-intensity lasers[13] or changes in the chemical composition of the environment.[9−12] ABF swimmers also have the potential to be functionalized and used as in vitro biomedical micro/nanorobots, and we have recently shown that helical propulsion is likely the best choice compared to other competing methods of magnetic propulsion once we consider the practical limitations in generating strong controlled magnetic fields.[14]

An ABF, developed as a device capable of controlled untethered locomotion in liquid, consists of two parts, a helical nanobelt tail resembling a natural flagellum in both size and shape and a soft-magnetic metal head in the shape of a thin square plate. The fabrication of an ABF is based

* To whom correspondence should be addressed. E-mail: (L.Z.) lizhang@ethz.ch; (B.J.N.) bnelson@ethz.ch.
† ETH Zurich.
‡ University of Utah.
§ Michigan State University.
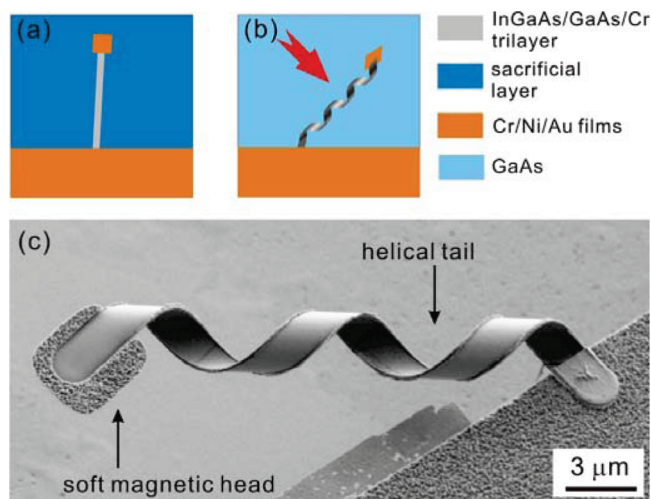
Figure 1. Fabrication of an ABF. (a) Using a "top-down" approach, an InGaAs/GaAs/Cr trilayer is patterned in a ribbon-like shape for the helical tail, and Cr/Ni/Au metal thin films are patterned for the soft-magnetic head of the ABF. (b) Wet etching of the sacrificial layer releases the 2D mesa forming a tethered ABF. The arrow indicates the scrolling direction, i.e., ⟨100⟩, on a (001) GaAs wafer. (c) SEM micrograph of an as-fabricated ABF with a diameter of 2.8 μm.

Figure 2. Dependence of ABF velocity on strength and rotation frequency of the applied magnetic field. Data are for a larger head, 38 μm long ABF swimming approximately horizontally. The error bars are attributed to the uncertainty in the position of the ABF based on the resolution of the recorded images.

on the self-scrolling technique.[15−18] After employing "top-down" fabrication processes, the entire 2D patterned mesa is released from the substrate and self-organizes to form a tethered ABF, as shown in Figure 1a,b. The details of the fabrication are reported elsewhere.[5] In the experiments, an ABF has an InGaAs/GaAs/Cr hybrid semiconductor-metal trilayer tail with thickness of 11/16/15 nm, respectively. The ribbon width is 1.8 μm, and the diameter of the as-fabricated ABF is 2.8 μm. The soft-magnetic metal head is in the shape of a thin square plate with dimensions of 4.5 μm (length) × 4.5 μm (width) × 200 nm (thickness) or 2.5 μm (length) × 2.5 μm (width) × 200 nm (thickness). It is composed of a Cr/Ni/Au trilayer with a thickness of 10/180/10 nm, respectively. We found that a thicker layer of evaporated Ni results in poor adhesion. Figure 1c shows a scanning electron microscopy (SEM) micrograph of an as-fabricated ABF. The geometrical shape of the helical tail (e.g., chirality, helicity angle, diameter, and length) can be precisely controlled.[17,18] The self-scrolling technique used allows the size of the 3D structure to be tuned from the nanometer to millimeter range by adjusting the layer thickness; furthermore, other materials can be integrated into the rolled-up structures.[16,19,20] To untether the ABF from the substrate, micromanipulation is performed to cut, pick, and release the ABF (see Supporting Information). Moreover, the length of the ABF tail can be tailored by micromanipulation as well.

Precise control of the motion of the ABF is achieved using three orthogonal electromagnetic coil pairs that generate a uniform rotating magnetic field (see Supporting Information). The control strategy for generating forward, backward, and steering motion is reported previously.[5]

The velocity of an ABF in water as a function of magnetic field strength and rotation frequency is characterized in Figure 2. A 38 μm long ABF with the larger head is used
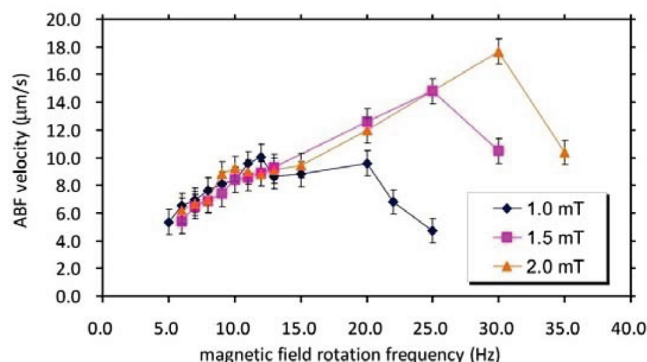
for the tests with three different field strengths, 1.0, 1.5, and 2.0 mT. The field's rotational frequency is increased from 5 to 35 Hz. To measure the velocity of the ABF under a particular magnetic field strength and frequency, we maintain the yaw and pitch[5] at a constant value. Since the ABF swims at a constant speed in a straight line, the displacement of the ABF divided by the swimming time yields velocity. The results show that at low frequency the swimmer's rotation is synchronized with the applied field, and ABF velocity increases linearly with frequency, as expected in the low-Reynolds-number regime.[1] After reaching a maximum value, the velocity reduces and becomes less deterministic with increasing field frequency, since the available magnetic torque is no longer sufficient to keep the swimmer synchronized with the applied field. This behavior is consistent with low-Reynolds-number experiments with macroscale helical swimmers.[21,22] The maximum synchronized frequency is referred to as the step-out frequency. The Reynolds number of the ABF in Figure 2 is in the range of 10^{-4} (the estimation of the Reynolds number of the ABFs are given in the Supporting Information) similar to the Reynolds number of bacteria in water.[6] The error bars in the Figure 2 are attributed to the uncertainty of the position of the ABF based on the resolution of the recorded images. The fluctuations in the curves are attributed to unmodeled boundary conditions such as wall effects[23−25] and intermolecular interactions of the ABF with the substrate. The maximum velocity that we have achieved with a 2.0 mT field is 18 μm/s, which is comparable to bacteria, such as *E. coli*, that swim by rotating their flagella with a frequency of about 100 Hz at room temperature.[26,27] It is notable that, since the *E. coli* bacteria are 1 order of magnitude smaller than the ABFs, the maximum relative velocity of the ABFs are not yet as high as *E. coli*, that is, ca. 10 body-length per second.[27] However, the results in Figure 2 also indicate that by exerting a stronger magnetic torque on the ABF, higher driving frequencies can be achieved resulting in higher linear velocity, and as expected, the maximum velocity is linearly proportional to the strength of the applied field.
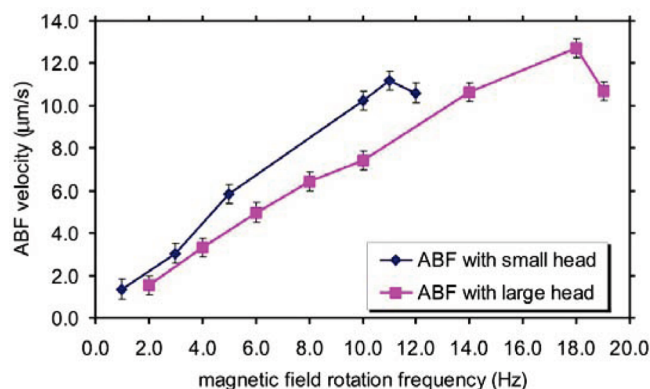
Figure 3. Dependence of ABF velocity on the size of the head. The strength of the magnetic field is 2 mT. (a) The ABF with a larger head (4.5 μm $\times$ 4.5 μm $\times$ 200 nm) has a smaller velocity than the ABF with a smaller head (2.5 μm $\times$ 2.5 μm $\times$ 200 nm). Both of the ABFs have 4.5 turns.
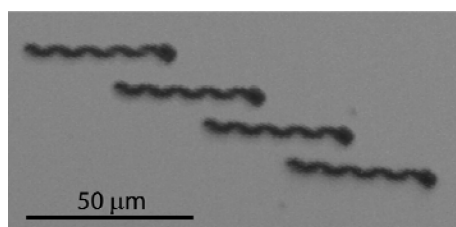
Figure 4. Time-lapse image showing drift due to the effect of a solid boundary (floor) below the ABF. As the ABF swims from left to right it drifts laterally (downward in the image).

For a comparison of the swimming velocity of ABFs with different head sizes, two 4.5-turn ABFs are tested in which one has a larger head and the other has a smaller head, as shown in Figure 3. The results show that the ABF with the small head swims faster than the ABF with the large head at low frequency. This is due to the increased forward viscous drag of a larger head with no additional benefit at low frequencies. However, because the ABF with a large head has a larger mass of Ni, a stronger magnetic torque can be generated, and we find that the step-out frequency and the maximum velocity increase with the large head. This result is consistent with the simulation results based on a simplified swimmer model (see Supporting Information). Realizing this increase in maximum velocity comes at the cost of generating higher-frequency rotating fields. The step-out frequency of the ABF with the large head in Figure 3 is much lower than that of the ABF in Figure 2, which is most likely due to oxidation of the Ni layer.[28]

Solid boundaries also affect ABF swimming. Rotating bodies tend to roll along solid boundaries, even when there is no direct contact, due to an increase in viscous drag near walls. It is known that some bacteria tend to swim in circles near solid boundaries, which is due to the counter-rotation of the bacterium body and its flagellum, each tending to roll along the wall in opposite directions, resulting in a net torque on the micro-organism.[29] We have observed an analogous behavior in ABFs. In Figure 4, we see a time-lapse image showing an ABF, which has sunk down toward the bottom
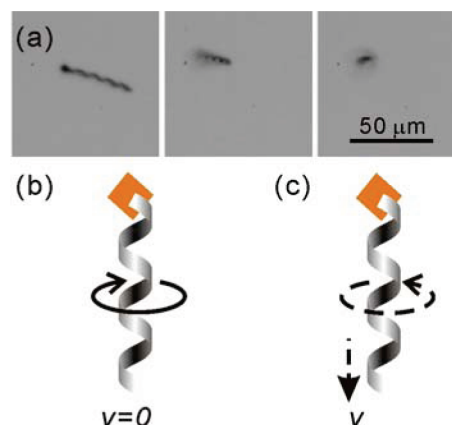
Figure 5. (a) Image sequence showing an ABF steered from horizontal to vertical (aligned with optical axis of microscope). (b) Schematic of the method to estimate the coefficient b in the propulsive matrix of an ABF. With a certain angular speed, the ABF has zero translation velocity, and the gravitational force of the ABF is counterbalanced by the sum of the propulsive force and the buoyant force of the ABF. (c) Schematic of the method to estimate the coefficient c in the propulsive matrix of the ABF. When the ABF falls due to the gravitational force, it rotates simultaneously.

of the reservoir, drifting laterally (downward in the image) as it advances from left to right. Because the magnetic head and the helical propeller do not counter-rotate, there is not a tendency for the ABF to swim in circles like a bacterium. In addition, the magnetic field induces a stabilizing (steering) torque to keep the ABF pointed in the desired direction. The drifting effect is reduced when the ABF moves farther from a solid boundary, and it disappears when the ABF swims vertically as shown in Figure 5a.

At a low Reynolds number regime, the nonfluidic applied torque[30] (τ) and the nonfluidic applied force[30] (F) on a helical swimmer are linearly related to its velocity (v) and angular speed (ω) with the four principle quantities described by a symmetric propulsion matrix:[1,6,7]

$$\begin{bmatrix} F \\ \tau \end{bmatrix} = \begin{bmatrix} a & b \\ b & c \end{bmatrix} \begin{bmatrix} v \\ \omega \end{bmatrix} \tag{1}$$

The sign convention is such that F and v are positive in the same direction, and τ and ω are positive in the same direction. Although experimental estimation of the propulsion matrix is challenging under an optical microscope, three separate experiments were conducted to estimate the three parameters sequentially. In the first experiment, the helical axis of a left-handed 38 μm long ABF with a large head is steered vertically, such that its direction is parallel to the optical axis of the microscope. A series of frames of this steering process is shown in Figure 5a. By adjusting the rotation frequency of the magnetic field, the ABF can swim upward or downward, depending on the balance between propulsive, gravitational, and buoyancy forces acting on the ABF. At a certain angular speed of the ABF, the sum of the propulsive force and the buoyant force balance the gravitational force as shown in Figure 5b, and the translational velocity becomes zero; this angular speed was measured as

Table 1. The Geometrical Parameters of the ABF

layer	ABF soft-magnetic head			ABF helical tail		
	Cr	Ni	Au	GaAs	$In_{0.14}Ga_{0.86}As$	Cr
density (g/cm³)	7.19	8.91	19.30	5.32	5.37	7.19
length (μm)	4.5	4.5	4.5	49.7	49.7	49.7
width (μm)	4.5	4.5	4.5	1.8	1.8	1.8
thickness (nm)	10	180	10	16	11	15
weight (pN)	1.4×10^{-2}	3.2×10^{-1}	3.8×10^{-2}	7.5×10^{-2}	5.2×10^{-2}	9.5×10^{-2}

5 Hz. The gravitational force of the ABF G_{ABF} is a sum of the weight of the helical tail and the soft-magnetic head, that is, $G_{ABF} = G_{tail} + G_{head}$. The weight of the helical tail and the soft-magnetic head is estimated by their density (ρ) and volume (V). According to the ABF parameters in Table 1, the gravitational force of the ABF is calculated as 0.59 pN and the buoyant force (F_b) due to water is calculated as $F_b = \rho_{water}gV = 0.077$ pN. The net nonfluidic applied force is the difference between the gravitational force and the buoyancy force, calculated as 0.51 pN. The nonfluidic applied force F is expressed as

$$F = av + b\omega \tag{2}$$

with $F = -5.1 \times 10^{-13}$ N, $v = 0$, and $\omega = 31$ rad/s, the coefficient b is calculated as -1.6×10^{-14} N·s. For the second experiment, the coefficient a in the propulsion matrix is derived from the velocity-angular speed curve as shown in Figure 2, in which the applied (axial) force is approximately equal to zero, since the ABF is swimming approximately horizontally. A linear fit is applied to the 2.0 mT data using all of the data up to the step-out frequency; a slope value of $v/\omega = 1.1 \times 10^{-7}$ m/rad is estimated. Using eq 2 with $F = 0$ and the calculated b value, the coefficient a is obtained as 1.5×10^{-7} N·s/m. In the final experiment, the coefficient c is estimated by another strategy in which the ABF swims vertically. In this experiment, after the ABF swims to the upper level of the water, the magnetic field is turned off and the ABF falls downward in the water due to gravity as it passively rotates, as depicted in Figure 5c. The experimental result shows that the ABF rotates approximately 80° within 4.9 s, thus the angular speed is calculated as $\omega = -0.28$ rad/s. The nonfluidic applied force is the difference between the gravitational force and the buoyant force, that is, $F = -5.1 \times 10^{-13}$ N, and the nonfluidic applied torque is 0. Thus, based on eq 2, the falling velocity of the ABF is calculated as $v = 4.1 \times 10^{-6}$ m/s. The nonfluidic applied torque is given by

$$\tau = bv + c\omega \tag{3}$$

Since the torque is equal to zero when the magnetic field is turned off, c is calculated as 2.3×10^{-19} N·m·s. Therefore, the propulsion matrix of the 38 μm long ABF is estimated as

$$\begin{bmatrix} a & b \\ b & c \end{bmatrix} = \begin{bmatrix} 1.5 \times 10^{-7} & -1.6 \times 10^{-14} \\ -1.6 \times 10^{-14} & 2.3 \times 10^{-19} \end{bmatrix} \tag{4}$$

From the velocity-angular speed curve shown in Figure 2, we can estimate the maximum magnetic torque that can be generated (τ_{max}) using the data at the step-out frequency values. For the field of 2.0 mT, the ABF has a maximum velocity of $v = 1.8 \times 10^{-5}$ m/s and a maximum angular speed of $\omega = 190$ rad/s. Using eq 3, the maximum magnetic torque (τ_{max}) is calculated as 4.3×10^{-17} N·m. We calculate the maximum pushing force (F_{max}) when the ABF moves in the horizontal plane by applying the maximum applied torque and setting $v = 0$, that is, $F_{max} = 3.0 \times 10^{-12}$ N.

The maximum pushing force of 3.0 pN at 2.0 mT is about 6 times larger than the net weight of the ABF in water. The maximum pushing force is linear with the strength of the applied magnetic field for this given ABF design and can be characterized by

$$\frac{F_{max}}{B} = 1.5 \times 10^{-9} \text{ N/T} \tag{5}$$

Moreover, the results show that the maximum pushing force with a 2.0 mT field is 3.0 pN, which is more than an order of magnitude larger than that of state-of-the-art nanomotors that use H_2O_2 as a fuel source.[10,11] The maximum torque is $\tau_{max} = 43$ nN·nm, which is approximately 2 orders of magnitude larger than that of the molecular motor in *E. coli*.[7] It is worth noting that, unlike artificial nanomotors or molecular motors in bacteria, the magnetic torque and
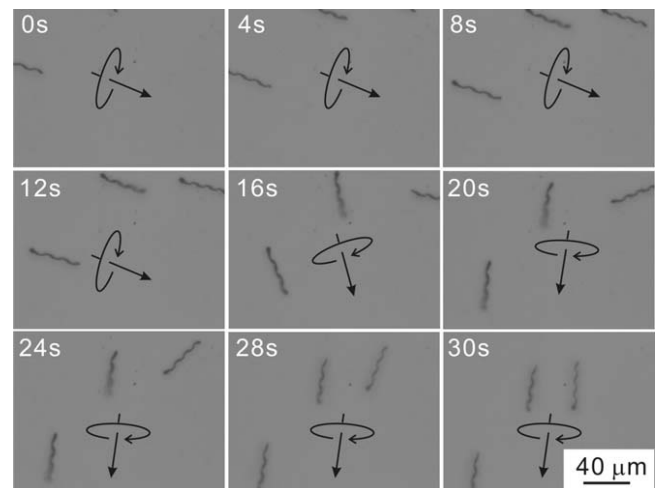
Figure 6. Swarm-like behavior of three ABFs controlled by rotating magnetic fields with 2 mT field strength. The group is controlled as a single entity with the commanded translation and rotation directions of the field indicated by the arrows. During a relatively fast steering movement, one ABF is temporarily separated from the group, but it naturally rejoins.

propulsive force of ABF can be tuned over a large range by controlling the parameters of the magnetic field and the design of the soft-magnetic head.

In Figure 6, we demonstrate simple swarm-like behavior in which three ABFs swim in a coordinated fashion. A video clip of this swarm-like behavior is also available in the Supporting Information. We find that the aggregate can be easily controlled as a single entity, and that ABF swimmers that become temporarily separated from the group due to complicated steering maneuvers return to the group without alteration of the rotating field. One of the ABFs did not follow the commanded steering temporarily, probably due to the fast steering speeds, yet it eventually rotates and swims in the same direction as the other two ABFs, although rotated by 180 degrees.

In contrast to bacteria that are propelled by natural flagella and move somewhat randomly in liquid, ABFs can be propelled and steered precisely in water by a low-strength, rotating magnetic field. The force and the torque can be estimated directly from the propulsion matrix once it is determined by experiments. These magnetically driven helical nanobelt devices can be used as wireless manipulators for medical and biological applications under 3D control in fluid environments, and they have the potential to perform manipulation with a full six degrees of freedom. Once functionalized, ABFs have the potential to sense and transmit inter- or intracellular information and to perform targeted delivery of energy (e.g., inductive heating) and of chemical and biological substances. ABFs also have the potential to be used in the human body as in vivo medical micro/nanorobots. However, tracking and navigation in a dynamic fluid environment will be challenging.

Supporting Information Available: Description of the ABF fabrication, the experimental setup, the micromanipulation of ABFs, the hydrodynamics simulation of dependence of head size on swimming velocity, as well as three video clips can be found online. Video S1 shows an ABF steered to swim in water in 3D, video S2 shows two ABFs swim forward while one is still tethered on the manipulator probe, and video S3 shows swarm-like behavior of ABFs. This material is available free of charge via the Internet at http://pubs.acs.org.

References

(1) Purcell, E. M. *Am. J. Phys.* **1977**, *45* (1), 3–11.
(2) Lighthill, J. *SIAM Review* **1976**, *18*, 161.
(3) Dreyfus, R.; Baudry, J.; Roper, M. L.; Fermigier, M.; Stone, H. A.; Bibette, J. *Nature* **2005**, *437*, 862–865.
(4) Berg, H. C.; Anderson, R. A. *Nature* **1973**, *245* (5425), 380–382.
(5) Zhang, L.; Abbott, J. J.; Dong, L. X.; Kratochvil, B. E.; Bell, D.; Nelson, B. J. *Appl. Phys. Lett.* **2009**, *94* (6), 064107.
(6) Purcell, E. M. *Proc. Natl. Acad. Sci. U.S.A.* **1997**, *94*, 11307.
(7) Chattopadhyay, S.; Moldovan, R.; Yeung, C.; Wu, X. L. *Proc. Natl. Acad. Sci. U.S.A.* **2006**, *103*, 13712–13717.
(8) Ghosh, A.; Fischer, P. *Nano Lett.* **2009**, *9* (6), 2243–2245.
(9) Burdick, J.; Laocharoensuk, R.; Wheat, P. M.; Posner, J. D.; Wang, J. *J. Am. Chem. Soc.* **2008**, *130* (26), 8164–8165.
(10) Sundararajan, S.; Lammert, P. E.; Zudans, A. W.; Crespi, V. H.; Sen, A. *Nano Lett.* **2008**, *8* (5), 1271–1276.
(11) Mei, Y. F.; Huang, G. S.; Solovev, A. A.; Urena, E. B.; Moench, I.; Ding, F.; Reindl, T.; Fu, R. K. Y.; Chu, P. K.; Schmidt, O. G. *Adv. Mater.* **2008**, *20* (21), 4085–4090.
(12) Solovev, A. A.; Mei, Y. F.; Urena, E. B.; Huang, G. S.; Schmidt, O. G. *Small* **2009**, *5* (14), 1688–1692.
(13) Ashkin, A.; Dziedzic, J. M. *Science* **1987**, *235* (4795), 1517–1520.
(14) Abbott, J. J.; Peyer, K. E.; Cosentino Lagomarsino, M.; Zhang, L.; Dong, L. X.; Kaliakatsos, I. K.; Nelson, B. J. *Int. J. Robot. Res.*, doi: 10.1177/0278364909341658.
(15) Prinz, V. Y.; Seleznev, V. A.; Gutakovsky, A. K.; Chehovskiy, A. V.; Preobrazhenskii, V. V.; Putyato, M. A.; Gavrilova, T. A. *Physica E* **2000**, *6* (1−4), 828–831.
(16) Schmidt, O. G.; Eberl, K. *Nature* **2001**, *410* (6825), 168–168.
(17) Zhang, L.; Deckhardt, E.; Weber, A.; Schonenberger, C.; Grutzmacher, D. *Nanotechnology* **2005**, *16* (6), 655–663.
(18) Zhang, L.; Ruh, E.; Grutzmacher, D.; Dong, L. X.; Bell, D. J.; Nelson, B. J.; Schonenberger, C. *Nano Lett.* **2006**, *6* (7), 1311–1317.
(19) Schmidt, O. G.; Schmarje, N.; Deneke, C.; Muller, C.; Jin-Phillipp, N. Y. *Adv. Mater.* **2001**, *13* (10), 756–759.
(20) Cho, A. *Science* **2006**, *313* (5784), 164–165.
(21) Honda, T.; Arai, K. I.; Ishiyama, K. *IEEE Trans. Magn.* **1996**, *32* (5), 5085–5087.
(22) Ishiyama, K.; Arai, K. I.; Sendoh, M.; Yamazaki, A. *J. Micromechatronics* **2003**, *2* (1), 77–86.
(23) Ramia, M.; Tullock, D. L.; Phanthien, N. *Biophys. J.* **1993**, *65* (2), 755–778.
(24) Frymier, P. D.; Ford, R. M.; Berg, H. C.; Cummings, P. T. *Proc. Natl. Acad. Sci. U.S.A.* **1995**, *92* (13), 6195–6199.
(25) Goto, T.; Nakata, K.; Baba, K.; Nishimura, M.; Magariyama, Y. *Biophys. J.* **2005**, *89* (6), 3771–3779.
(26) Berg, H. C.; Brown, D. A. *Nature* **1972**, *239* (5374), 4.
(27) Berg, H. C. *E. coli in Motion*; Springer: New York, 2004.
(28) The experiments for $v-\omega$ plots of Figure 2 are approximately 7 months earlier than those of Figure 3 but with the same batch of ABFs.
(29) Lauga, E.; DiLuzio, W. R.; Whitesides, G. M.; Stone, H. A *Biophys. J.* **2006**, *90* (2), 400–412.
(30) We refer to "nonfluidic applied force" and "nonfluidic applied torque" as forces and torques experienced by the ABFs that are not generated by fluid drag effects.

NL901869J